

DECARBONIZATION BUILDING IMPROVEMENT

Tej Jolly, Shawn Krishnan, [Vedant Singh](#)
tkj, shawnakk, vhsingh

ABSTRACT

This report focuses on optimizing decarbonization building designs to reduce atmospheric CO₂. Using computational fluid dynamics (CFD) simulations, we analyzed airflow patterns and carbon-depleted air re-entrainment under various building configurations. Our parametric study used finite difference methods, fractional step approaches, and advection-diffusion solvers to model velocity, pressure, and species transport. Our parametric studies revealed the influence of building dimensions and wind profiles on decarbonization efficiency, with findings suggesting that taller and narrower structures minimize re-entrainment. Our analysis included controlled wind profiles and species transport to identify optimal configurations within a fixed area. While the study is limited by 2D geometry and static wind patterns, the results provide valuable insights for designing efficient decarbonization facilities. Future work will incorporate 3D simulations and dynamic environmental conditions to enhance the robustness of these findings.

INTRODUCTION AND BACKGROUND

Decarbonization buildings are engineered to intake ambient air, extract carbon dioxide (CO₂), and expel carbon-depleted air, which will reduce atmospheric CO₂ levels. However, their efficiency is compromised by re-entrainment, where expelled decarbonized air is drawn back into the intake. This phenomenon is exacerbated under unfavorable wind conditions, and reduces the effectiveness of CO₂ removal.

We conducted a literary review of modern approaches to optimize building design in an effort to guide our problem solving with our CFD analysis. In the building and construction industry, the integration of Building Information Modeling (BIM) with Computational Fluid Dynamics (CFD) has become a standard approach for designing efficient structures. BIM provides a framework for visualizing, analyzing, and optimizing building performance, while CFD enables precise simulations of airflow and environmental interactions. For example, Kang et al. (2022) reviewed BIM-CFD integration and highlighted its applications in energy assessment, HVAC

system design, and sustainable infrastructure. This combined approach has advanced the industry, but challenges such as interoperability and high computational costs remain areas for further research.

While advanced tools like BIM offer comprehensive solutions, our project focuses on a simplified yet effective approach using CFD simulations to analyze decarbonization buildings. Specifically, we investigate the impact of building geometry and intake/outlet airflow speeds on re-entrainment during adverse wind conditions. By narrowing our scope, we aim to model the fundamental principles governing re-entrainment and provide actionable insights into optimizing decarbonization facility designs.

Additional studies have laid the groundwork for understanding airflow dynamics around structures. Alam (2023) developed a CFD-based tool for optimizing carbon capture enclosures, underscoring the importance of airflow efficiency. Similarly, "Computational Fluid Dynamics for Built and Natural Environments" (2019) highlighted the role of CFD in solving building aerodynamics problems, while parametric studies on air-cooled chiller compounds demonstrated how design considerations can mitigate re-entrainment. These studies provide critical context for our work.

This report expands on these insights to tackle the specific challenges associated with decarbonizing buildings. Using CFD simulations, we investigate the interaction between wind conditions, building geometry, and airflow patterns to identify configurations that minimize re-entrainment and optimize efficiency. Our simplified methodology complements the industry-standard BIM-CFD integration by targeting key design parameters, providing actionable solutions to advance decarbonization efforts.

PROBLEM SETUP

The objective of this study is to analyze the airflow dynamics around decarbonization buildings and identify configurations that minimize the re-entrainment of carbon-depleted air under adverse wind conditions. Re-entrainment occurs when expelled air is drawn back into the intake, reducing the building's CO₂ removal efficiency. To address this issue, we conducted CFD

simulations to evaluate the influence of building geometry and intake/outlet airflow speeds on re-entrainment. The achievable quantity of decarbonization per facility depends on the volume of limestone reserve within the facility.. Therefore, in 2-D, we will hold area constant for different building variations.

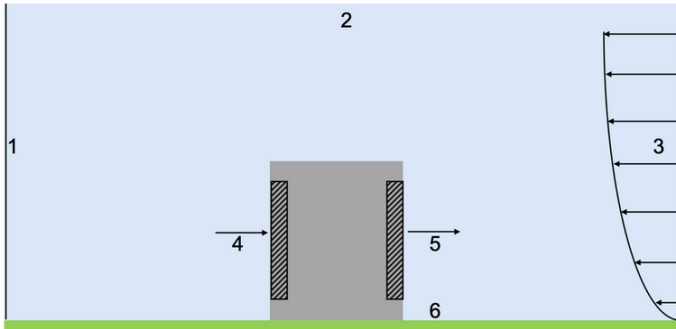
PROBLEM DOMAIN AND BOUNDARY CONDITIONS

The simulation domain includes a decarbonization building placed in a controlled airflow environment. The computational domain is bounded by several Dirichlet and no-slip boundary conditions:

TABLE 1: Boundary Conditions

Boundary Condition	Boundary Number
Pressure Outlet (0 Gauge Pressure)	1
Pressure Outlet (0 Gauge Pressure)	2
Velocity Inlet defined by Power-Law	3
Wind Profile	
Velocity Inlet for the decarbonization intake	4
Velocity Outlet with specified velocity magnitude	5
No Slip	6

FIGURE 1: Boundary Conditions



The building's geometry and boundary conditions were chosen to reflect real-world operational conditions. The dimensions of the building were varied to maintain a constant area, allowing a parametric study of its height and width's impact on re-entrainment.

NUMERICAL FORMULATION

In our solver we used 5 numerical techniques, those being the fractional step method, the finite difference method, the pressure poisson equation, the scalar transport method, and SOR.

The fractional step method was used in time marching by separating the velocity and pressure fields to solve the

Navier-Stokes equations iteratively.

We start with two momentum equations which are solved without the pressure gradient term to compute intermediate velocities (u^* and v^*).

$$\begin{aligned} u^* &= u^n + \Delta t (-\partial/\partial x(uu) - \partial/\partial y(uv) + v\nabla^2 u) \\ v^* &= v^n + \Delta t (-\partial/\partial x(uv) - \partial/\partial y(vv) + v\nabla^2 v) \end{aligned}$$

Next we use the pressure poisson equation (PPE) to update the pressure field and ensure incompressibility:

$$\nabla^2 p = (\rho/\Delta t)(\partial u^*/\partial x + \partial v^*/\partial y)$$

Finally, we use the updated pressure field to calculate the updated velocity fields.

$$\begin{aligned} u^{n+1} &= u^* - \Delta t (\partial p / \partial x) \\ v^{n+1} &= v^* - \Delta t (\partial p / \partial y) \end{aligned}$$

In these equations ν represents the kinematic viscosity.

The next method we used was the finite difference method

A combination of upwind schemes and central differencing were used for stability and accuracy. We used Upwind for stability in nonlinear convection terms and Central differencing for diffusive terms.

$$(\partial u^2 / \partial x)_i \approx (u_i + u_{i+1})^2 - (u_{i-1} + u_i)^2 / (4\Delta x)$$

For diffusion terms we used second-order central differencing.

$$\nabla^2 u = ((u_{i+1,j} - 2u_{i,j} + u_{i-1,j}) / (\Delta x^2)) + ((u_{i,j+1} - 2u_{i,j} + u_{i,j-1}) / (\Delta y^2))$$

For the temporal discretization we used explicit schemes for convective and viscous terms in the predictor step. The timestep (Δt) is dynamically calculated using the CFL conditions and diffusion limiting.

$$\Delta t = 0.9 \cdot \min(\Delta x / |u|, \Delta y / |v|)$$

The time step is constrained by the equation, and the minimum value is selected.

$$\Delta t_{\text{diff}} = \Delta x^2 / 4\nu$$

For the pressure poisson equation we used successive over-relaxation using a factor of ω . Our boundary conditions ensure physical consistency. The inlet velocity is specified, the outlet has a zero-gradient for the velocity and zero gauge pressure, and the walls have no slip conditions.

$$\begin{aligned} p_{i,j} &= 0.25 * (p_{i+1,j} + p_{i-1,j} + p_{i,j+1} + p_{i,j-1}) \\ &- \Delta x^2 / \rho \Delta t ((u_{i,j} - u_{i-1,j}) / \Delta x + (v_{i,j} - v_{i,j-1}) / \Delta y) \end{aligned}$$

SOR Relaxation:

$$p_{i,j(k+1)} = (1-\omega)p_{i,j}^{(k)} + \omega \cdot \text{rhs}$$

For scalar transport we used the scalar transport equation with v_c as the diffusion coefficient. The equation was discretized using an upwind scheme to ensure stability and prevent numerical oscillations.

$$c_{i,j}^{n+1} = c_{i,j}^n - \Delta t (u \cdot \partial c / \partial x + v \cdot \partial c / \partial y) + \Delta t v_c \nabla^2 c$$

The re-entrainment ratio, R , was defined as the fraction of inlet air flux composed of exhaust air, mathematically expressed as:

$$R = pcu\Delta y / \rho u \Delta y$$

where ρ is the density of air, c is the concentration of the scalar (exhaust species), u is the horizontal velocity component, and Δy is the vertical height of the inlet region.

RESULTS AND DISCUSSION SECTION

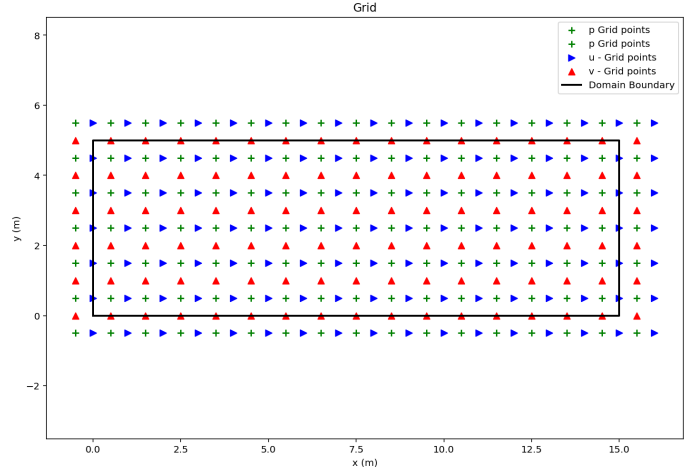
We tested multiple configurations of our design using rectangles with inlet and outlet points holding them all to a constant area of 200 m². The configurations are listed in the table below.

TABLE 2: Building Configurations

Configuration Width (m)	Configuration Height (m)
25	8
20	10
10	20
8	25

The computational domain was discretized using a staggered Cartesian mesh with uniform grid spacing in both the x and y directions. The mesh resolution was chosen to balance accuracy and computational efficiency, with cell sizes set to $\Delta x = 1$ m and $\Delta y = 1$ m. This uniform grid ensured consistent resolution across the domain, capturing critical flow features such as wake formation and recirculation zones. The building geometry and obstacle regions were explicitly resolved within the mesh to accurately model the impact of airflow interactions. We used dynamic timestepping that satisfied CFL conditions, to maintain numerical stability.

FIGURE 2: Mesh Grid



We then successively added a wind profile, power law wind profile, building, and building with active intake and exhaust, ensuring each modification to the flow field matched expectations.

FIGURE 3: Constant Wind Profile

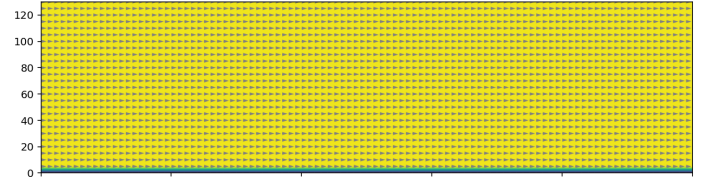
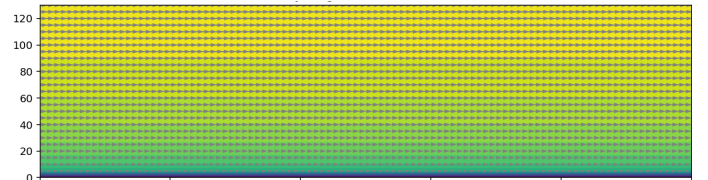


FIGURE 4: Power Law Wind Profile



Figures 3 and 4 compare the effects of two different wind profiles on airflow dynamics: a constant wind profile (top) and a power-law wind profile (bottom). The constant wind profile assumes uniform velocity across the height, while the power-law profile incorporates a realistic velocity gradient, with lower speeds near the ground and increasing speeds at higher altitudes. The power-law profile demonstrates a more accurate representation of atmospheric boundary layer behavior. The power law wind profile is crucial in determining building efficiency as it is what we are testing against.

FIGURE 4: Velocity Profile with building

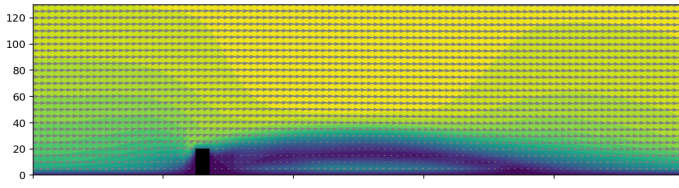
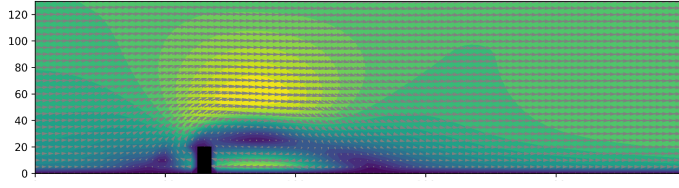


FIGURE 5: Velocity Profile with building and intake



Figures 4 and 5 illustrate the velocity profiles for two configurations: one with only the building present (Figure 3) and the other with the building and an intake system (Figure 4). In Figure 4, the flow remains relatively undisturbed downstream of the building, with minimal recirculation zones. However, in Figure 5, the introduction of an intake system creates pronounced changes in the velocity field, with significant recirculation and flow redirection near the intake. These results emphasize how building design and intake placement influence airflow patterns and potentially affect re-entrainment of carbon-depleted air.

FIGURE 6: Species Transport

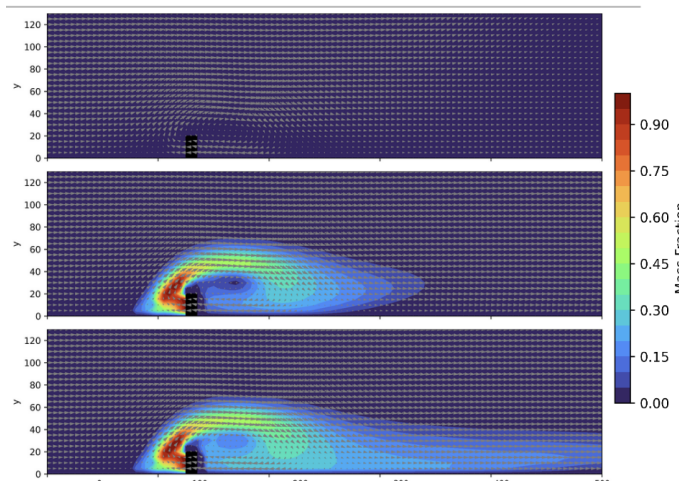


Figure 6 is a series of plots that demonstrates the mass fraction transport of carbon-depleted air under different stages of re-entrainment. The top plot shows the initial airflow velocity vectors, highlighting the general flow direction around the building. In the middle plot, the concentration of carbon-depleted air becomes evident, with clear regions of recirculation forming near the outlet. These regions indicate where re-entrainment occurs as expelled air begins to flow back toward the intake. The bottom plot reveals the sustained impact of building geometry and airflow interaction on the distribution of carbon-depleted air, showing a pronounced overlap between

the outlet and intake streams.

Below are the 10m (width) by 20m (height) velocity profiles at multiple times ($t = 0, 220, 605, 818$) seconds.

FIGURE 7: Velocity Profile $t = 0$ s (10x20) Configuration

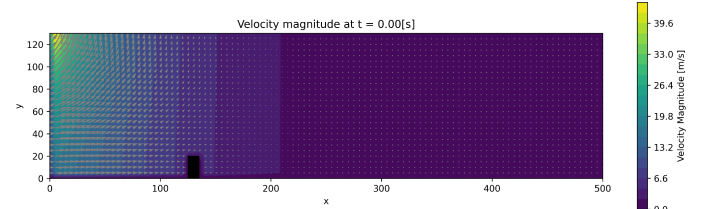


FIGURE 8: Velocity Profile $t = 220$ s (10x20) Configuration

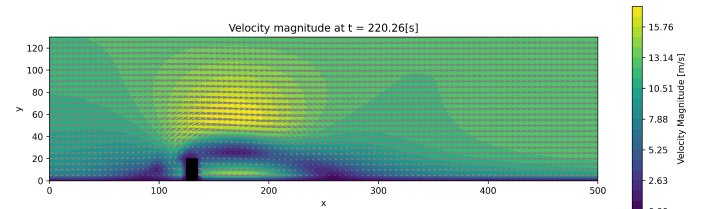


FIGURE 9: Velocity Profile $t = 605$ s (10x20) Configuration

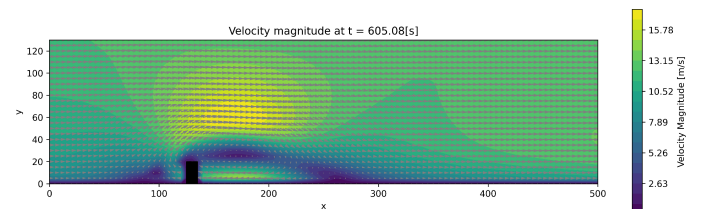
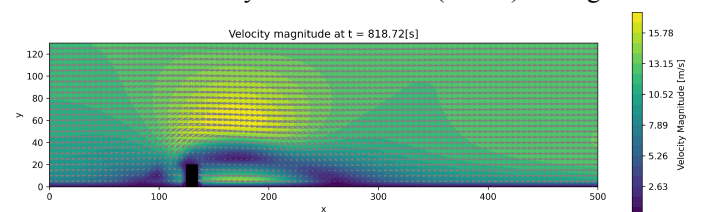


FIGURE 10: Velocity Profile $t = 818$ s (10x20) Configuration



Figures 7-10 show the evolution of the velocity magnitude profile for the 10x20 configuration over time. At $t = 0$ s (Figure 7), the velocity field is uniform, with no significant flow disturbances caused by the building. By $t = 220$ s (Figure 8), the interaction between the airflow and the building begins to create separation zones near the intake and outlet, as well as a developing wake downstream. At $t = 605$ s (Figure 9), the flow stabilizes further, with a well-defined wake region and noticeable velocity gradients near the building. By $t = 818$ s (Figure 10), the flow reaches a steady state, with the wake and separation zones fully formed..

FIGURE 11: Pressure Profile $t = 0$ s (10x20) Configuration

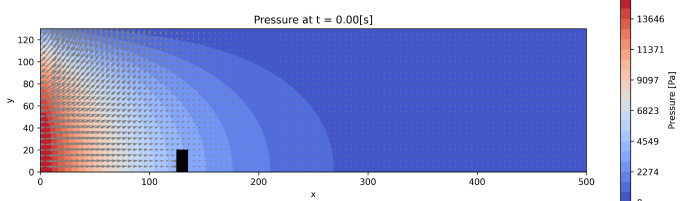


FIGURE 12: Pressure Profile $t = 220\text{s}$ (10x20) Configuration

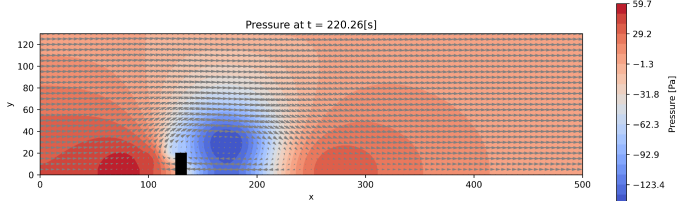


FIGURE 13: Pressure Profile $t = 605\text{s}$ (10x20) Configuration

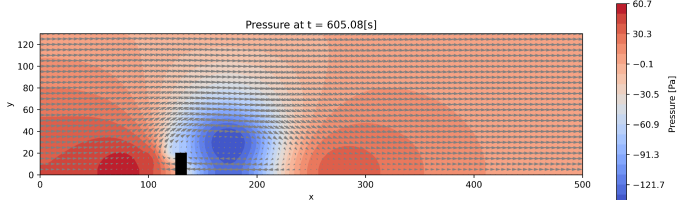
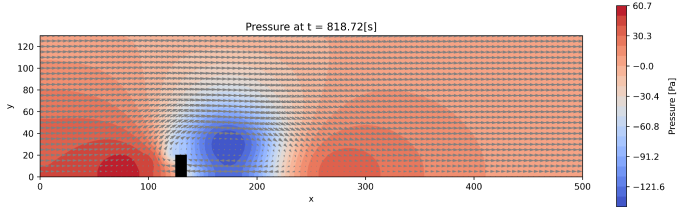


FIGURE 14: Pressure Profile $t = 818\text{s}$ (10x20) Configuration



Figures 11-14 illustrate the pressure profile evolution for the 10x20 configuration at the same time steps. At $t = 0\text{s}$ (Figure 11), the pressure field is uniform, dominated by high pressure upstream of the building. By $t = 220\text{s}$ (Figure 12), a distinct low-pressure region begins to form near the outlet, with localized gradients around the intake and the wake region. At $t = 605\text{s}$ (Figure 13), the pressure distribution stabilizes, showing a strong low-pressure zone behind the building and high-pressure regions upstream. By $t = 818\text{s}$ (Figure 14), the pressure profile reflects a steady state with well-defined zones of pressure disparity that directly influence airflow direction and re-entrainment efficiency. These findings demonstrate the role of pressure gradients in driving re-entrainment and highlight how the inlet and outlet influence these pressure zones.

FIGURE 15: U-Velocity $t = 0\text{s}$ (10x20) Configuration

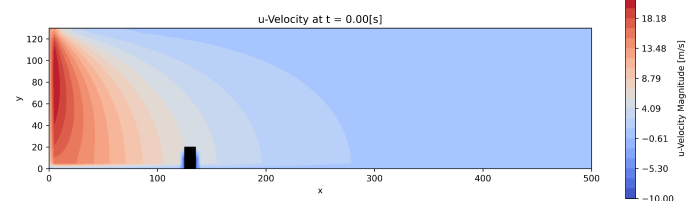


FIGURE 16: U-Velocity $t = 605\text{s}$ (10x20) Configuration

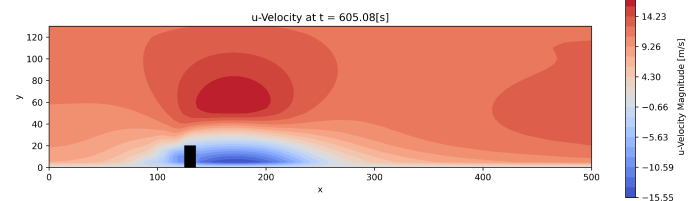
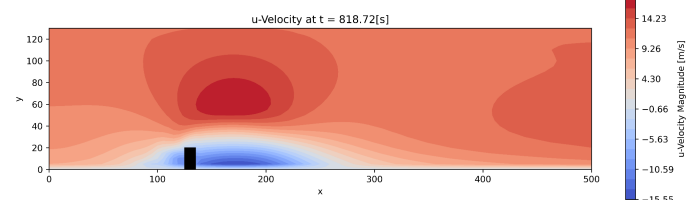


FIGURE 17: U-Velocity $t = 818\text{s}$ (10x20) Configuration



The following plots show the scalar concentrations across the simulation domain.

FIGURE 18: Mass Fraction $t = 0\text{s}$ (10x20) Configuration

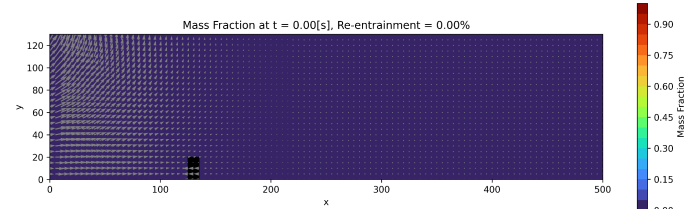


FIGURE 19: Mass Fraction $t = 0\text{s}$ (10x20) Configuration

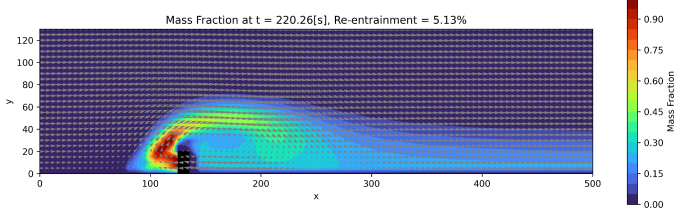


FIGURE 20: Mass Fraction t = 0s (10x20) Configuration

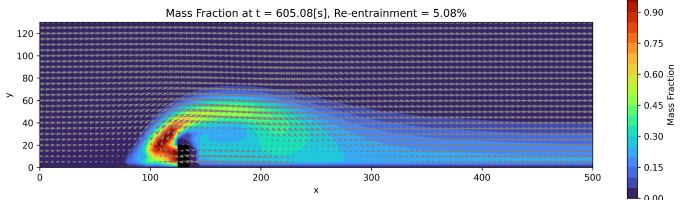
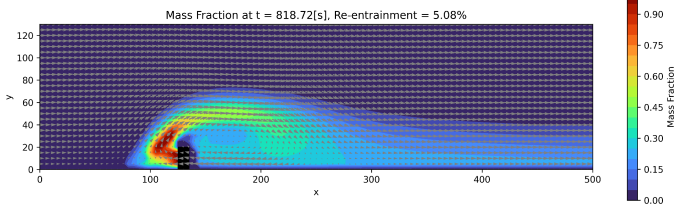


FIGURE 21: Mass Fraction t = 0s (10x20) Configuration



Figures 18-21 show the progression of mass fraction for the given conditions in the 10x20 configuration over time. At t = 0s (Figure 18), there is no re-entrainment, with mass fraction uniformly distributed near zero. By t = 220s (Figure 19), a re-entrainment percentage of 5.13% is observed, as carbon-depleted air begins to interact with the intake region. This trend stabilizes at t = 605s and 818s (Figures 20 and 21), with re-entrainment percentages maintaining around 5.08%. These results indicate that the 10x20 configuration effectively minimizes re-entrainment, with the low percentage of 5% signifying a highly efficient design for maintaining intake air purity.

Using the 10x20 configuration as a benchmark we aim to compare this re-entrainment percentage information with other configurations. Namely the inverse 20x10 as well as a different ratio at the same total area 8x25, and 25x8.

FIGURE 22: Steady State Velocity Profile (20x10)

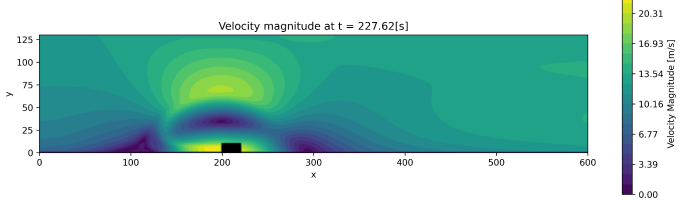


FIGURE 23: Steady State Pressure Profile (20x10)

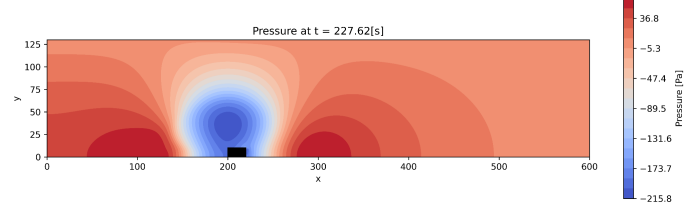
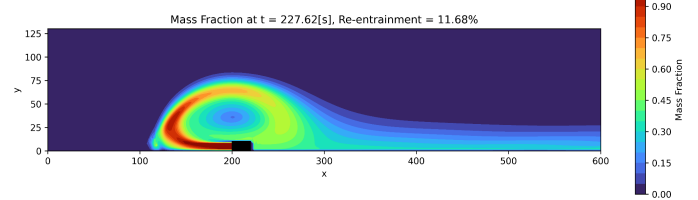


FIGURE 24: Steady State Mass Fraction (20x10)



Figures 22-24 illustrate the steady-state velocity, pressure, and mass fraction profiles for the 20x10 configuration. The velocity profile (Figure 22) shows a more significant spread of airflow around the building, indicating less vertical confinement and greater horizontal dispersion. This results in a broader low-pressure zone observed in Figure 23, with pressure minima extending further upstream and downstream compared to the 10x20 configuration.

The mass fraction profile (Figure 24) reveals a re-entrainment percentage of 11.68%, more than double the 5% observed in the 10x20 configuration. This higher re-entrainment is attributed to the wider structure's geometry, which allows greater overlap between the outlet and intake streams. In contrast, the taller 10x20 configuration provides better vertical separation, minimizing re-entrainment and maintaining higher decarbonization efficiency.

We continue with the same analysis on the remaining two configurations.

FIGURE 25: Steady State Velocity Profile (8x25)

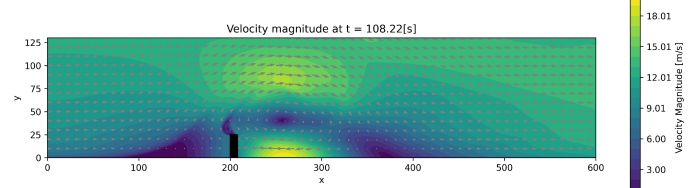


FIGURE 26: Steady State Pressure Profile (8x25)

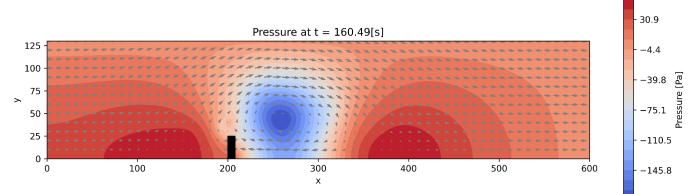
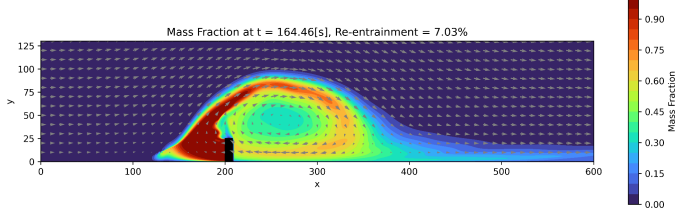


FIGURE 27: Steady State Velocity Profile (8x25)



Figures 25–27 present the steady-state velocity, pressure, and mass fraction profiles for the 8x25 configuration. Compared to the 10x20 and 20x10 configurations, this geometry demonstrates an intermediate level of performance in terms of re-entrainment, which is measured at 7.03% in Figure 27. This is lower than the 20x10 configuration but higher than the 10x20 configuration.

The velocity profile (Figure 25) shows a moderate spread of airflow, with some confinement near the building but less vertical separation compared to the taller 10x20 structure. The pressure distribution (Figure 26) exhibits a localized low-pressure zone near the building, with less pronounced upstream effects than the 20x10 configuration. This contributes to better separation of intake and outlet streams but still allows some overlap. Overall, the 8x25 configuration represents a compromise between vertical separation and horizontal dispersion, with reduced but not minimized re-entrainment.

FIGURE 28: Steady State Velocity Profile (25x8)

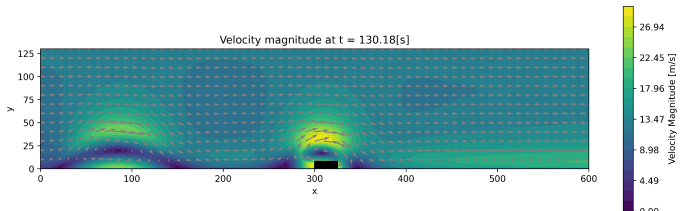


FIGURE 29: Steady State Pressure Profile (25x8)

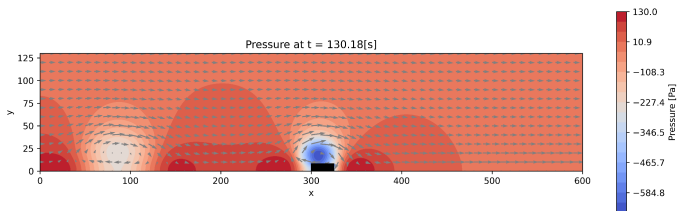
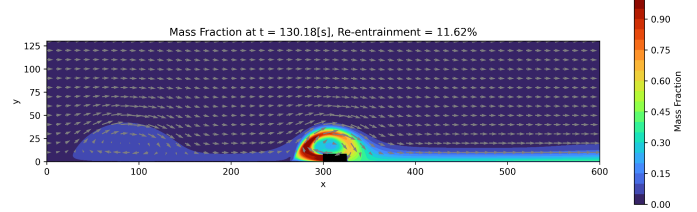


FIGURE 30: Steady State Mass Fraction (25x8)



The 25x8 configuration (Figures 28–30) demonstrates a distinct shift in airflow and mass fraction dynamics compared to previous configurations. The velocity profile (Figure 28) reveals a pronounced downward deflection of flow near the intake, indicating strong interaction between the inlet and outlet streams. The pressure profile (Figure 29) highlights a concentrated low-pressure region directly above the outlet, facilitating increased re-entrainment. The mass fraction plot (Figure 30) shows a re-entrainment percentage of 11.62%, which is higher than the narrower configurations such as 8x25 (7.03%) but comparable to the 20x10 (11.68%) setup. This underscores that while a wider configuration can improve lateral dispersion, it is less effective at maintaining separation between intake and outlet flows, ultimately leading to higher re-entrainment percentages.

All steady-states were verified by plotting the solver and assessing whether or not the solution had sufficiently converged. Figure 31 illustrates the convergence behavior of the pressure solver over successive timesteps, showing the number of iterations required for convergence. As the simulation progresses, the number of iterations decreases sharply, indicating that the flow has stabilized and the pressure fields are reaching a fully developed state. Beyond timestep 30, the number of iterations flattens, suggesting that the solver has reached steady convergence, and the flow fields are fully developed. This trend confirms that the computational framework achieves stability and efficiency in capturing the steady-state behavior of the system. Each configuration had varying converging times which is why there is a noticeable difference in the time in the plots from figures 22–30.

FIGURE 31: Convergence 10x20 Configuration

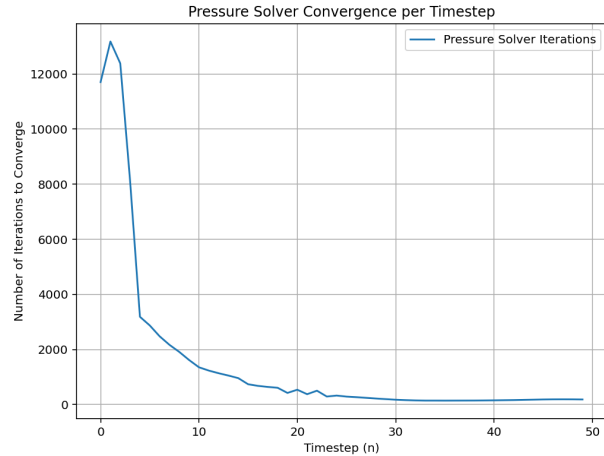


TABLE 3: Convergence 10x20 Configuration

Configuration	Re-entrainment %
25x8	11.62
8x25	7.03
20x10	11.68
10x20	5.08

Table 3 provides a summary of the re-entrainment percentages for the parametric study.

After conducting our steady-state analysis, we now turn to interpreting the observed re-entrainment percentages and their implications for decarbonization efficiency. The results from the scalar transport simulations, velocity fields, and pressure distributions clearly illustrate how building geometry influences the degree to which exhaust air is reintroduced into intake streams. In particular, the velocity field analyses (Figures 6–9, 22, 25, and 28) reveal that taller, narrower building configurations, such as the 8x25 structure (with a height-to-width ratio of 3.125:1), create more streamlined airflow. This streamlined flow reduces turbulence in the wake region and effectively separates intake and exhaust paths. Notably, the 8x25 configuration achieved one of the lowest re-entrainment rates—7.03%—underscoring its strong potential for minimizing the recirculation of carbon-depleted air. By contrast, wider configurations, like the 20x10 (1:2 height-to-width ratio), displayed larger and more turbulent wake zones, resulting in a higher re-entrainment rate of 11.68%. These findings challenge the initial assumption that shorter, wider designs would mitigate low pressure zones leeward of the building; instead, they affirm that streamlined, vertically oriented structures better reduce re-entrainment.

The pressure distribution patterns (Figures 10–13, 23, and 26) further highlight the significance of building geometry in governing re-entrainment. Narrower configurations generate

smaller adverse pressure gradients, thereby diminishing the strength of recirculation regions behind the building. In contrast, wider setups amplify these pressure differences, creating more pronounced low-pressure areas in the wake and, consequently, worsening re-entrainment. For instance, the 20x10 configuration, which yielded moderate yet still substantial re-entrainment (11.68%), demonstrates how geometry-driven pressure gradients can directly contribute to downstream turbulence and subsequent contamination of intake streams.

The scalar transport simulations (Figures 18–21, 24, 27, and 30) provided a more direct measure of these effects by quantifying re-entrainment rates and linking them to CO₂ capture efficiency. Here again, the 8x25 structure proved notably effective, registering one of the lowest re-entrainment rates (7.03%), while the 20x10 configuration struggled with significant overlap between intake and outlet streams, thereby reducing overall efficiency. Interestingly, the 25x8 configuration (also 3.125:1 but with the orientation reversed) had a re-entrainment rate of 11.62%, indicating that while proportions matter, orientation and other geometric factors likewise influence performance.

The parametric examination (summarized in Table 2) systematically varied height-to-width ratios while maintaining a constant building area. This survey consistently demonstrated that taller designs outperformed wider ones in reducing re-entrainment and enhancing CO₂ capture. For example, a 4:1 height-to-width ratio achieved approximately 8% re-entrainment, illustrating the clear advantages of such proportions. Still, these improvements must be weighed against practical considerations, including construction costs and structural stability.

Taken together, these findings underscore the critical importance of optimizing building geometry to reduce turbulence, manage pressure gradients, and improve the efficiency of decarbonization efforts. While the data strongly favor taller, narrower designs, further studies involving three-dimensional modeling and dynamic environmental conditions will be necessary to fully validate these insights and refine guidelines for real-world applications. Such work may also explore hybrid solutions that combine tall core structures with strategically optimized outlets, aiming to balance enhanced operational efficiency with practical feasibility on a large scale.

SUMMARY AND CONCLUSIONS

- Decarbonization buildings are designed to intake ambient air, extract CO₂, and expel carbon-depleted

- air, with efficiency often compromised by re-entrainment of expelled air.
- Literature reviews highlight the role of CFD and BIM in optimizing building designs, with CFD providing precise airflow simulations to address challenges like re-entrainment.
 - Simulations demonstrate that taller and narrower configurations, such as 10x20 and 8x25, minimize re-entrainment (5.08% and 7.03%, respectively) by reducing turbulence and promoting streamlined airflow.
 - Wider configurations, like 20x10 and 25x8, show higher re-entrainment rates (11.68% and 11.62%) due to overlapping intake and exhaust flows and significant wake turbulence.
 - Reduced adverse pressure gradients in taller designs lead to minimized recirculation zones, enhancing decarbonization efficiency and maintaining air purity.
 - The parametric study confirms that increasing the height-to-width ratio consistently lowers re-entrainment and maximizes CO₂ capture efficiency, despite practical challenges like structural stability.
 - Future work will incorporate 3D simulations and dynamic environmental conditions to validate these findings and refine real-world decarbonization building designs.

REFERENCES

1. Singh, S. (2024). *Computational Fluid Dynamics (24-718)* [Course lectures]. Carnegie Mellon University.
2. Kang, K.-Y., Wang, X., Wang, J., Xu, S., Shou, W., & Sun, Y. (2022). Utility of BIM-CFD Integration in the Design and Performance Analysis for Buildings and Infrastructures of Architecture, Engineering and Construction Industry. *Buildings*, 12(5), 651. [MDPI](#)
3. Alam, M. S. (2023). A Computational Fluid Dynamics-based Design Optimization Tool for Carbon Capture Enclosure. *Applied Research Consortium*.
4. Parametric Study of Air Re-entrainment within Air-Cooled Chiller Compounds. (2019). *Proceedings of Building Simulation 2019*.
5. Optimization of Building Wind Environment Using CFD and Genetic Algorithms. (2023). *IEEE Xplore*.
6. Computational Fluid Dynamics for Built and Natural Environments. (2019). *Springer*.